

# Structural changes across thermodynamic maxima in supercooled liquid tellurium: a water-like scenario?

Peihao Sun,<sup>1,2,\*</sup> Giulio Monaco,<sup>2</sup> Peter Zalden,<sup>3</sup> Klaus Sokolowski-Tinten,<sup>4</sup> Jerzy Antonowicz,<sup>5</sup> Ryszard Sobierajski,<sup>6</sup> Yukio Kajihara,<sup>7</sup> Alfred Q. R. Baron,<sup>8</sup> Paul Fuoss,<sup>1</sup> Andrew Chihpin Chuang,<sup>9</sup> Jun-Sang Park,<sup>9</sup> Jonathan Almer,<sup>9</sup> and J. B. Hastings<sup>1,†</sup>

<sup>1</sup>*SLAC National Accelerator Laboratory, 2575 Sand Hill Rd, Menlo Park, CA 94025, USA*

<sup>2</sup>*Dipartimento di Fisica e Astronomia “Galileo Galilei”,*

*Università degli Studi di Padova, Via F. Marzolo, 8, 35131 Padova, Italy*

<sup>3</sup>*European XFEL, Holzkoppel 4, 22869 Schenefeld, Germany*

<sup>4</sup>*Faculty of Physics and Center for Nanointegration Duisburg-Essen (CENIDE),*

*University of Duisburg-Essen, Lotharstrasse 1, 47048 Duisburg, Germany*

<sup>5</sup>*Faculty of Physics, Warsaw University of Technology, Koszykowa 75, Warsaw, 00-662, Poland.*

<sup>6</sup>*Institute of Physics of the Polish Academy of Sciences, PL-02-668 Warsaw, Poland*

<sup>7</sup>*Graduate School of Advanced Science and Engineering,*

*Hiroshima University, Higashi-Hiroshima, Hiroshima 739-8521, Japan*

<sup>8</sup>*Materials Dynamics Laboratory, RIKEN SPring-8 Center, 1-1-1 Kouto, Sayo, Hyogo 679-5148, Japan*

<sup>9</sup>*X-ray Science Division, Advanced Photon Source,*

*Argonne National Laboratory, Lemont, Illinois 60439, USA*

(Dated: January 19, 2022)

Liquid polymorphism is an intriguing phenomenon which has been found in a few single-component systems, the most famous being water. By supercooling liquid Te to more than 130 K below its melting point and performing simultaneous small-angle and wide-angle X-ray scattering measurements, we observe clear maxima in its thermodynamic response functions around 615 K, suggesting the presence of liquid polymorphism. A close look at the underlying structural evolution shows the development of intermediate-range order upon cooling, most strongly around the thermodynamic maxima, which we attribute to bond-orientational ordering. The striking similarities between our results and those of water indicate that water-like anomalies and the liquid-liquid transition can be a general phenomenon among systems with competing bond- and density-ordering.

## I. INTRODUCTION

Liquid polymorphism, or the existence of two or more liquid phases of the same substance, is a topic of much current interest [1, 2]. Although the concept dates back to at least the 1960s [3], supporting evidence had been lacking until recent years, when observations of phenomena related to liquid polymorphism began to emerge in a variety of systems. Perhaps the most intriguing among these are single-component systems, where the polymorphism points out the insufficiency of the theory of simple liquids [4] to describe real, albeit compositionally simple, fluid systems, while suggesting the strong influence of local structures even for the properties of amorphous materials. The current list of systems with clear experimental evidence for a liquid-liquid transition (LLT), in decreasing complexity, includes large molecules such as triphenyl phosphite [5] and atomic systems such as phosphorus [6, 7], sulfur [8], and cerium [9]. Meanwhile, an LLT has been suggested in many other systems with varying degrees of experimental and theoretical evidence [2].

Among these systems, water is perhaps the most famous. It is well-known that water exhibits a number of thermodynamic anomalies such as a density maximum at

4 °C under ambient pressure. Among the different scenarios explaining water’s anomalies [10, 11], the second critical point hypothesis [12] has emerged as a leading theory, supported in particular by recent results from both experiments [13, 14] (although not without controversy [15, 16]) and simulations [17, 18]. Under this framework, there exists an LLT in water in the deeply supercooled region and under elevated pressures, and the coexistence line of this LLT terminates at a liquid-liquid critical point (LLCP). A peculiar aspect of the LLT in liquid water, distinguishing it from most other systems, is the fact that the low-density liquid phase lies on the low temperature side of the transition. While this explains the density maximum in a straightforward way [11, 12], it also leads to the distinctive phase diagram where the LLT exists at higher pressures than the LLCP, thus setting water apart from other single-component systems mentioned above. In addition, the critical pressure is predicted to be positive but not far from zero, so thermodynamic effects related to critical fluctuations can be observed along the  $P \approx 0$  isobar [13]. These effects manifest as maxima in thermodynamic response functions such as the isothermal compressibility, and they form a line emanating from the LLCP usually referred to as the Widom line [19]. For ordinary water (H<sub>2</sub>O), evidence suggests that the Widom line intersects the  $P \approx 0$  isobar around 229 K [13]. A schematic phase diagram proposed for water is shown in Fig. S1.

\* Corresponding author: peihao.sun@unipd.it

† Corresponding author: jbh@slac.stanford.edu

In general, the physical origin of water’s peculiarities is not entirely clear, and it remains an open question whether they are unique to water or are general to a family of liquids. In fact, it has been suspected that other tetrahedrally coordinated systems (such as silicon) exhibit similar behaviors [20, 21]. Another candidate is liquid tellurium (Te), whose lack of tetrahedrality makes it a somewhat surprising example. As observed first by Kanno et al. [22] and reiterated by Angell [23], liquid Te also exhibits a variety of thermodynamic anomalies which bear a striking resemblance to those of water. A systematic study of the properties of liquid Te thus can be informative on the universality of water-type LLT, bearing significance from a fundamental physics aspect. From a practical point of view, Te is the basis element of phase-change materials (PCMs) that are becoming increasingly important for information technology [24]. Thus, it is reasonable to expect that the phenomena attributed to liquid polymorphism in PCMs [25] are related to the possible LLT in liquid Te.

Therefore, in this work, we study the properties of bulk supercooled liquid Te under low vapor pressure ( $< 0.5$  mbar). We are able to achieve supercooling by more than 130 K below its melting point of 723 K and observe maxima in various thermodynamic response functions including the isothermal compressibility. Moreover, we are able to determine details of the structural changes across the Widom line, which show many similarities with water. Our results clearly show that intermediate-range ordering plays a central role in the structural modification, and indicate that water-like thermodynamic anomalies may be attributed to a competition between density and bond-ordering regardless of the details of the local structure.

## II. SIMULTANEOUS SAXS AND WAXS

In order to systematically study the thermodynamic and structural changes, we performed simultaneous small-angle and wide-angle X-ray scattering (SAXS and WAXS) measurements at beamline 1-ID at the Advanced Photon Source. The high X-ray photon energy, 76.112 keV, allows us to probe bulk Te samples in a simple transmission geometry. See Materials and Methods for details.

Our dataset includes three scans. The scans are temporally separated during the experiment, performed on different samples, and the X-ray beam condition differs between the scans. The consistency of the results from all scans, as will be shown below, strongly supports our conclusions. Each scan consists of several rounds of temperature cycling, where in each round the sample is first heated above its melting point and then cooled down in steps (usually 10 K) to the lowest temperature. At each step, after temperature equilibration, X-ray scattering patterns are collected for several minutes. Recrystallization happens suddenly and can be identified by the ap-

pearance of sharp Bragg peaks in the WAXS pattern; these data are excluded in the analysis.

Figure 1 shows the WAXS and SAXS results from scan 1. The structure factor  $S(Q)$  is obtained from the WAXS patterns, and the results agree well with those in the literature (see Supplementary Materials). Several trends can be clearly observed. Firstly, with cooling, the first peak moves to lower  $Q$  values, which is similar to the behavior of water [13, 26]. The second peak becomes sharper while its position remains relatively constant at  $3.3 \text{ \AA}^{-1}$ . The broad third peak spanning 4 to  $6 \text{ \AA}^{-1}$  gradually changes its symmetry upon cooling, with the low- $Q$  side centered around  $4.4 \text{ \AA}^{-1}$  decreasing in magnitude and the high- $Q$  side centered around  $5.1 \text{ \AA}^{-1}$  growing. Remarkably, the same phenomenon has been observed in *ab initio* molecular dynamics (AIMD) simulations [27], although the growth of the high- $Q$  side becomes obvious there only at the very low temperature of 560 K.

An interesting feature is the presence of the pre-peak centered around  $1.4 \text{ \AA}^{-1}$ , as shown with a magnified view in the upper panel of the inset. To better visualize this pre-peak, we fit an exponential function,  $S(Q) = Ae^{aQ} + B$  ( $A, a, B$  are fit parameters), to the regions below and above it ( $0.9$  to  $1.1 \text{ \AA}^{-1}$  and  $1.6$  to  $1.8 \text{ \AA}^{-1}$ ) as the baseline, and the fit results are shown as dashed lines. The lower panel of the inset shows the pre-peak region with the baseline subtracted, where we can clearly see its growth in magnitude and its movement to slightly lower  $Q$  upon cooling (quantitative results presented in Supplementary Materials). We note that a pre-peak is also observed in Te-based chalcogenides such as  $\text{Ge}_{15}\text{Te}_{85}$  [28–31], as well as phase-change materials [32] particularly in the supercooled liquid region. In these materials, the appearance of the pre-peak is attributed mostly to the Ge atoms [29] and explained as a Peierls-like distortion [30, 31]. Here in pure Te, the pre-peak is found to exist above the melting point as well, where the liquid is metallic [33]. Therefore, a Peierls-like distortion is unlikely, while it is possible that the pre-peak arises from bond-orientational order, as will be discussed later.

For SAXS, as in most other atomic liquids, the structure factor of liquid Te is much less than unity and the scattering is weak. Consequently, the background is significant and its pattern depends on the position of the sample and the furnace, and thus it is difficult to be measured and subtracted accurately. Nonetheless, within each scan, sample movement is negligible and the background pattern is expected to remain unchanged. Therefore, for the SAXS analysis we calculate the change in the structure factor,  $\Delta S(Q)$ , from the highest temperature in each scan, which cancels out the background. For scan 1, this is 733 K, above the melting point at 723 K. The results are shown in Fig. 1b, and they show unambiguously a non-monotonic behavior with cooling: while  $\Delta S(Q)$  increases at first, it begins to decrease at the lowest temperatures. To quantify the change, as in earlier works on chalcogen systems [34], we fit a linear function to  $\Delta S(Q)$  with the results shown as dashed lines. The ex-

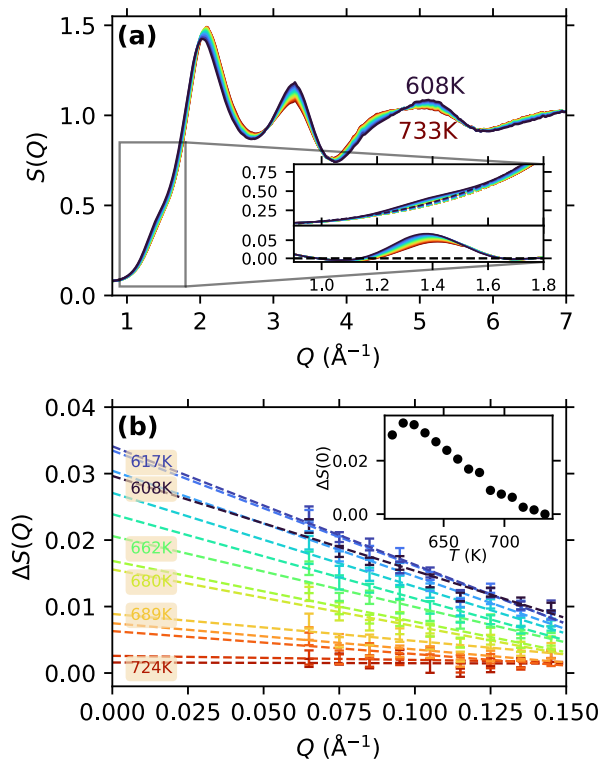


FIG. 1. (a) Te WAXS profiles (structure factor  $S(Q)$ ) from scan 1. From dark red to dark blue are decreasing temperatures; the highest and lowest temperatures are indicated. Inset: upper panel shows the details of the pre-peak around  $1.4 \text{ \AA}^{-1}$  (solid lines) and the baseline (dashed lines) obtained by fitting the data before and after the pre-peak; lower panel shows the pre-peak with the baseline subtracted. (b) Te SAXS profiles from the same scan, subtracting the highest temperature profile (733 K) in the scan. The color scheme is the same as in (a). Data are shown with error bars, and the dashed lines show linear fits to the data. Several temperatures are marked next to the fit lines with the corresponding colors. Inset shows the intercept  $\Delta S(0)$  plotted against sample temperature; the error bars are smaller than the symbol.

tracted intercept,  $\Delta S(0)$ , is plotted against temperature in the inset, and a peak can be clearly observed. This suggests the existence of thermodynamic maxima to be discussed below.

### III. MAXIMA IN THE THERMODYNAMIC RESPONSE FUNCTIONS

The non-monotonic behavior in the SAXS region bears much resemblance to recent results on supercooled water [13], where it is found to associate with the liquid-liquid transition. We now look further into the extent of similarities between the two systems. The density maximum at  $4 \text{ }^\circ\text{C}$  is often thought to be a salient anomaly of water. Figure 2 shows our results from all three scans on the density of supercooled liquid Te obtained with X-

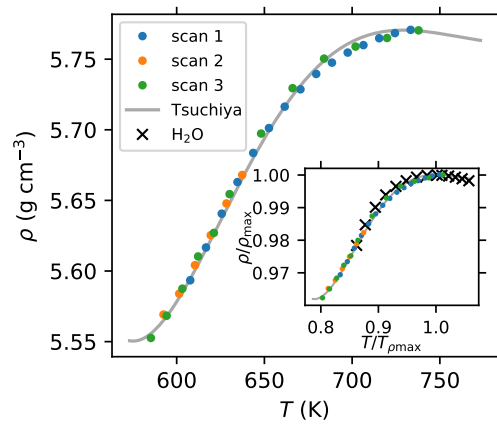


FIG. 2. Density of liquid Te plotted against temperature. Dots with different colors show results from the three different scans, which agree well with each other and with the data reported by Tsuchiya [35] (gray line). Inset shows the same data in reduced temperature and density, which are normalized by the location of density maximum  $\rho_{\max} = 5.77 \text{ g/cm}^3$  around  $T_{\rho_{\max}} = 729 \text{ K}$ . Black crosses show the results on supercooled [36] and normal liquid water [37], which bear remarkable resemblance to Te.

ray transmission measurements (see Supplementary Materials). The results are consistent between scans, and all agree well with the values previously reported by Tsuchiya [35]. The inset shows the same data plotted on reduced scales normalized by the maximum density  $\rho_{\max} = 5.77 \text{ g/cm}^3$  and the corresponding temperature  $T_{\rho_{\max}} = 729 \text{ K}$ . When the available data on water is plotted on the same reduced scale (with  $\rho_{\max} = 1 \text{ g/cm}^3$  and  $T_{\rho_{\max}} = 277 \text{ K}$ ), a remarkable resemblance between the two systems can be observed, as has been pointed out in the literature [22, 23].

As in the case of water [11], the density anomaly in liquid Te suggests the existence of liquid polymorphism. To provide further evidence for this scenario, in Fig. 3 we show, with colored symbols representing different scans, four properties of liquid Te: (a) the  $Q \rightarrow 0$  limit of the structure factor,  $S(0)$ , (b) the isothermal compressibility,  $\kappa_T \equiv -V^{-1}(\partial V/\partial P)_T$ , (c) the temperature derivative of the position of the first peak,  $Q_{m1}$ , and (d) the opposite of the thermal expansion coefficient  $\alpha_P \equiv V^{-1}(\partial V/\partial T)_P$ . Of these quantities,  $Q_{m1}$  can be obtained from the WAXS data in a straightforward way, and  $\alpha_P$  can be derived from the density measurement shown above. To obtain  $S(0)$  and  $\kappa_T$ , we use the following relation [38]:

$$S(0) = k_B T \frac{\rho}{m} \kappa_T, \quad (1)$$

where  $k_B$  is the Boltzmann constant and  $m$  is the mass of the Te atom. For  $S(0)$ , the value at the highest temperature for each scan is determined using Eq. (1) and a known value of  $\kappa_T$ : for scans 1 and 3, this is above the melting point and we use the value given in Ref. [35];

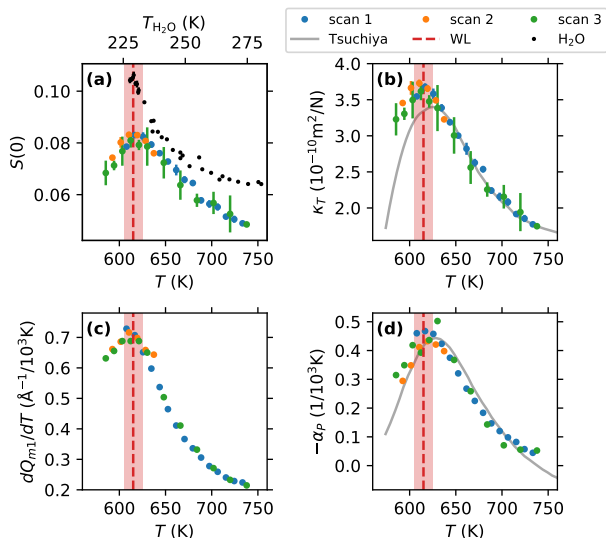


FIG. 3. Properties of supercooled Te and evidence for the Widom line. (a)  $S(0)$ , (b) isothermal compressibility,  $\kappa_T$ , (c) temperature derivative of the first peak position,  $Q_{m1}$ , and (d) the opposite of the thermal expansion coefficient  $\alpha_P$ , all plotted against sample temperature  $T$ . Results by Tsuchiya [35] are shown as gray lines in (b) and (d). The vertical dashed line shows the approximate position of the Widom line, 615 K, and the red shaded region indicate a  $\pm 10$  K range around it as a guide to the eye. In (a) we also plot  $S(0)$  for water (small black dots, upper  $x$ -axis) [13].

for scan 2, we use the results from the other two scans. Because we have measured the relatively change  $\Delta S(0)$  from the highest temperature, the values of  $S(0)$  and  $\kappa_T$  are then obtained. The presence of maxima is evident in all panels of Fig. 3. For  $S(0)$  and  $\kappa_T$  we note that, although the procedure described above is used to obtain their absolute values, the maxima can already be seen in  $\Delta S(0)$  as shown in Fig. 1b as well as Figs. S10b and S11b in Supplementary Materials. The approximate position of the maxima, 615 K, is marked with a dashed vertical line in Fig. 3, while the shaded region indicates a  $\pm 10$  K range as a guide to the eye.

The existence and the shape of these maxima provide crucial information on the thermodynamics of liquid Te, in particular the possible morphology of its liquid phase diagram, which has not been discussed much in the literature. Given the similarities between the thermodynamic properties of Te and water, however, it is reasonable to refer to studies on the latter, of which an extensive amount exist. Specifically, to explain water’s thermodynamic anomalies, most of which are shared by Te, four scenarios have been proposed [10, 11]: i) the “retracting spinodal” scenario [39], where the anomalies are consequences of the liquid-vapor spinodal re-entering the supercooled liquid region; ii) the LLC scenario [12], where the anomalies are effects in the vicinity of the critical point; iii) the “hidden critical point” scenario [40], where the LLC is located outside the liquid-vapor spinodal;

iv) the “singularity free” scenario, where the LLC is inaccessible either because it is located at  $T = 0$  K [41, 42] or because the critical density is too high to achieve [43]. For liquid Te, the maxima observed in Fig. 3 rule out scenario i which predicts divergence due to the spinodal [39], while the breadth of these maxima and the continuous change in the structure factor (e.g.,  $Q_{m1}$ ) excludes scenario iii where a first-order LLT is expected [40]. Thus, we are left with the LLC scenario ii and the singularity-free scenario iv. Although the present results do not fully exclude scenario iv, it should be mentioned that the thermodynamic maxima in singularity-free models can still be described using the concept of the Widom line emanating from an inaccessible LLC [42, 43]. In particular, as will be discussed below, they signify a rapid crossover between two liquid structures just as in the LLC scenario. Therefore, in the discussions below we use the language of liquid polymorphism, particularly the LLC and the Widom line, to describe and interpret our results.

Further evidence for the similarity between Te and water can be seen in Fig. 3a, where the measured values of  $S(0)$  in supercooled water [13] are also shown. Note that  $S(0)$  is a dimensionless quantity reflecting the number fluctuations in the system [38]:

$$S(0) = \frac{\langle (N - \langle N \rangle)^2 \rangle}{\langle N \rangle}, \quad (2)$$

where  $N$  is the number of particles (Te atoms or water molecules) in a given sample volume and the angular brackets denote the ensemble average. Thus, the fact that  $S(0)$  is close in magnitude between Te and water at  $P \approx 0$  indicates that the critical pressure in liquid Te may be as close to zero pressure as in water.

#### IV. STRUCTURAL CHANGES

Pertinent to the phenomenon of liquid polymorphism is the underlying structural transformation between the different liquid forms. The WAXS data, with examples given in Fig. 1a, allows us to examine the microscopic structural changes across the thermodynamic maxima in detail. Our experimental setup provides data up to  $Q = 7 \text{\AA}^{-1}$ , and previous works have shown that little change appears in  $S(Q)$  beyond  $6 \text{\AA}^{-1}$  across a range of 500 K [27, 44]. Therefore, we append literature data from 7 to  $15 \text{\AA}^{-1}$  [27, 45] to our results to obtain the radial distribution function  $g(r)$  (further details in Supplementary Materials), which describes the average density at a distance  $r$  from a reference atom. In Fig. 4a, we show the function  $r^2 g(r)$  with cooling from 738 K to 585 K. Two salient features emerge: a decrease in the region between  $\sim 3 \text{\AA}$  and  $\sim 3.7 \text{\AA}$ , and an increase in the broad second peak around 3.7 to 4.7  $\text{\AA}$ . In Fig. 4b we plot the running coordination number,  $N(r)$ , which is obtained from  $g(r)$  and represents the averaged number of atoms within a distance  $r$  from the reference atom. Indeed, the change in  $N(r)$  is small up to  $R_1 = 3.14 \text{\AA}^{-1}$ , where the data

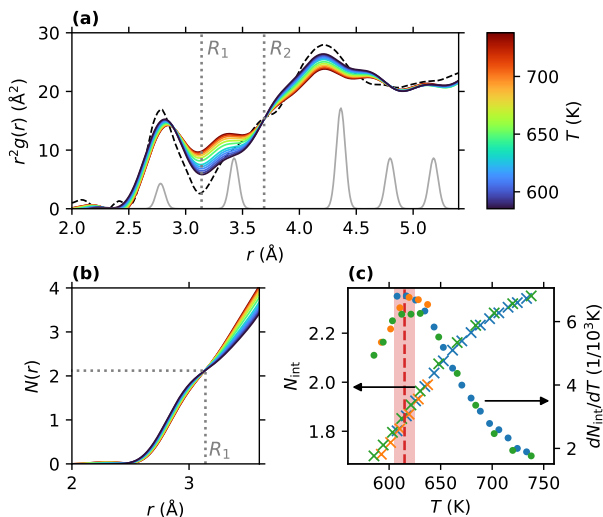


FIG. 4. Temperature evolution of the structure of liquid Te. From dark red to dark blue the temperature decreases from 738 K to 585 K, as shown in the color bar. (a) shows the function  $r^2g(r)$  and (b) shows the running coordination number  $N(r)$ . Also shown in (a) are trigonal Te [50] (gray solid line) and electron diffraction results on amorphous Te [46] (black dashed line). Vertical lines: we take  $R_1$ , the isosbestic point in (b), as the boundary of the first shell;  $R_2$  is a near-isosbestic point in (a) and is taken to be the lower boundary of the second shell. (c) shows the number of atoms in the intermediate region (crosses, left  $y$ -axis) between  $R_1$  and  $R_2$  for all three scans, as well as its temperature derivative (dots, right  $y$ -axis). The derivative shows a maximum near the Widom line (dashed vertical line).

appears to have an isosbestic point. We thus take  $R_1$  to be the boundary of the first coordination shell, resulting in a coordination number of approximately 2.1 under all temperatures. Remarkably, the position of  $R_1$  also lies close to the first minimum in  $g(r)$  of amorphous Te [46], as shown in Fig. 4a, which further supports this choice of  $R_1$  as the boundary of the first shell.

Here we note that earlier works attributed the structural transition in liquid Te to a decrease of coordination number from 3 to 2 upon cooling [33]. However, this model has been much debated in the literature [47], and it was pointed out that the measured coordination number depends sensitively on both the exact definition of the first shell boundary [48] and the available  $Q$  range [49]. In fact, more recent AIMD results [27] show that even the trend depends on the cutoff radius of the first shell: if the cutoff is at 3.1 Å, the coordination number increases with cooling, while it decreases with a cutoff at 3.2 Å. Notably, this is consistent with our observation that the coordination number remains constant with a cutoff around 3.14 Å, leading to the conclusion that the coordination number alone does not explain the behavior of supercooled Te.

The plots shown in Figs. 4a and 4b bear a notable resemblance to recent measurements on water [26]. In

particular, an isosbestic point was also found in the running coordination number  $N(r)$  of water, leading to the conclusion that the first shell coordination is mostly constant from 300 K down to 244.2 K [26]. In addition, a depletion of molecules was found upon supercooling in the region between the first and second peak, referred to as the interstitial region [26]. This means that for both water and Te, intermediate-range ordering instead of changes in first-shell coordination drives the structural changes upon cooling and possibly distinguishes the two liquid structures: the high-temperature liquid is dominated by a denser and more disordered structure, including more interstitial atoms, while the low-temperature liquid is dominated by a less dense and more ordered structure up to the second shell.

To quantify the structural changes in liquid Te, we calculate the rate of depletion of atoms in between the first and second peaks, hereinafter referred to as the intermediate region. The lower boundary of this intermediate region is the first shell boundary  $R_1$ , while we define the upper cutoff  $R_2$  as the near-isosbestic point observed in  $r^2g(r)$ , around  $3.69 \text{ \AA}^{-1}$ . Although this choice of  $R_2$  is somewhat arbitrary, small changes do not alter the conclusions below (see Supplementary Materials). We can then obtain the number of atoms between  $R_1$  and  $R_2$ ,  $N_{\text{int}}$ , as a function of temperature. The results are plotted as crosses in Fig. 4c, and  $N_{\text{int}}$  increases with temperature as expected. Further, the temperature derivative of  $N_{\text{int}}$  can be obtained, as shown in the same panel, and it shows a peak similar in both position and shape to the maxima in Fig. 3. This provides strong evidence that the thermodynamic changes in Fig. 3 are accompanied by a fast depletion of atoms in the intermediate region, signifying an increase in intermediate-range ordering.

## V. DISCUSSION AND CONCLUSIONS

The results above have shown clear evidence for rapid intermediate-range ordering across the Widom line in supercooled Te, but details of this ordering remain to be discussed. Here we propose that bond-orientational order plays a crucial role. The pre-peak in Fig. 1a, centered around  $Q_{pp} = 1.4 \text{ \AA}^{-1}$ , signals the presence of some structure on the order of  $2\pi/Q_{pp} = 4.5 \text{ \AA}$ . In the crystal, this corresponds to the distance between next-nearest neighbors within a chain (i.e., the third peak of trigonal Te in Fig. 4a), whose bonds with their common neighbor form an angle of  $103.2^\circ$  [50]. The second peak in the liquid  $g(r)$  is also close to  $4.5 \text{ \AA}$ , but slightly lower in  $r$ , indicating a somewhat smaller average bond angle consistent with AIMD results [27]. With decreasing temperatures, we observe a growth of the pre-peak by almost 60% (see Fig. 1a and Supplementary Materials), while AIMD shows that the bond-angle distribution becomes sharply peaked around  $96^\circ$  [27]. In addition, the AIMD results have shown that two-coordinated atoms (within a soft cutoff around 3.2 Å) have a bond angle distribution

which is strongly peaked around  $100^\circ$ , whereas atoms with higher coordination show a broader bond-angle distribution peaked close to  $90^\circ$  [27]. This suggests that an increase in bond-orientational order would lead to a decrease in atoms in the intermediate region, as we have observed.

The similarities between Te and water in the various aspects we have discussed are worth emphasizing for several reasons. Firstly, the thermodynamic similarities indicate that the liquid phase diagrams of Te and water are likely similar. Thus, investigations into one may provide vital information for the other. Secondly, the similarities between the structural evolution of the two indicate a common microscopic origin. Our results confirm that a reduction in atoms in the intermediate region between the first and second peaks in  $g(r)$ , similar to the depletion of interstitial atoms observed in water [26], indeed accompanies the transition across the Widom line in liquid Te; such data is not yet available in water due to difficulties in reaching the deep supercooled state. Last but not least, the observed similarities strongly indicate that the anomalies of water are not limited to systems with hydrogen bonding or tetrahedral coordination, but are general to a family of liquids. Indeed, the enhanced intermediate-range ordering in the low-temperature limit is consistent with the two-state model [2, 51], where the thermodynamic anomalies (such as the density maximum) are caused by the increase in locally favored, albeit less dense, structures upon cooling. Since the presence of locally favored structures are expected in a number of liquids [2], it is reasonable to predict that more systems can be found to exhibit water-type anomalies. Studying the commonalities and differences between these systems may help reveal the role of intermediate-range structures and bond-orientational ordering in the behavior of liquids.

In conclusion, using a combination of small-angle and

wide-angle X-ray scattering, we have observed clear indications of the Widom line in supercooled liquid Te as well as the structural changes that accompany it. Our results suggest that intermediate-range ordering, likely of a bond-orientational nature, is strongly associated with the anomalous properties of liquid Te and underlies the phenomena of liquid polymorphism in this system. Moreover, the striking resemblance between Te and water in various properties, in spite of their different local structures, points to the possible existence of water-like thermodynamic anomalies in a family of liquid systems. Thus, our study suggests that the competition between bond- and density-ordering can be a general phenomenon and plays a crucial role in the thermodynamics of liquid systems.

## ACKNOWLEDGMENTS

We thank Charles L. Troxel Jr. for his tremendous help during preparation for the experiment. We also thank Ali Mashayekhi for his valuable support during the experiment. This research used resources of the Advanced Photon Source, a U.S. Department of Energy (DOE) Office of Science User Facility at Argonne National Laboratory and is based on research supported by the U.S. DOE Office of Science-Basic Energy Sciences, under Contract No. DE-AC02-06CH11357. This work is supported by the U.S. Department of Energy, Office of Science, Office of Basic Energy Sciences under Contract No. DE-AC02-76SF00515; the Deutsche Forschungsgemeinschaft (DFG, German Research Foundation) through the Collaborative Research Centre (CRC) 1242, project number 278162697; and the National Science Centre, Poland, grant agreement No. 2017/27/B/ST3/02860.

- 
- [1] H. E. Stanley, ed., *Liquid Polymorphism*, Advances in Chemical Physics (John Wiley & Sons, Inc., Hoboken, NJ, USA, 2013).
  - [2] H. Tanaka, Liquid-liquid transition and polyamorphism, *The Journal of Chemical Physics* **153**, 130901 (2020).
  - [3] E. Rapoport, Model for Melting-Curve Maxima at High Pressure, *The Journal of Chemical Physics* **46**, 2891 (1967).
  - [4] J.-P. Hansen and I. R. McDonald, *Theory of Simple Liquids*, 3rd ed. (Academic Press, London, 2006).
  - [5] R. Kurita and H. Tanaka, Critical-Like Phenomena Associated with Liquid-Liquid Transition in a Molecular Liquid, *Science* **306**, 845 (2004).
  - [6] Y. Katayama, T. Mizutani, W. Utsumi, O. Shimomura, M. Yamakata, and K. Funakoshi, A first-order liquid-liquid phase transition in phosphorus, *Nature* **403**, 170 (2000).
  - [7] G. Monaco, S. Falconi, W. A. Crichton, and M. Mezouar, Nature of the First-Order Phase Transition in Fluid Phosphorus at High Temperature and Pressure, *Physical Review Letters* **90**, 255701 (2003).
  - [8] L. Henry, M. Mezouar, G. Garbarino, D. Sifré, G. Weck, and F. Datchi, Liquid-liquid transition and critical point in sulfur, *Nature* **584**, 382 (2020).
  - [9] A. Cadien, Q. Y. Hu, Y. Meng, Y. Q. Cheng, M. W. Chen, J. F. Shu, H. K. Mao, and H. W. Sheng, First-Order Liquid-Liquid Phase Transition in Cerium, *Physical Review Letters* **110**, 125503 (2013).
  - [10] G. Pallares, M. El Mekki Azouzi, M. A. Gonzalez, J. L. Aragoes, J. L. F. Abascal, C. Valeriani, and F. Caupin, Anomalies in bulk supercooled water at negative pressure, *Proceedings of the National Academy of Sciences* **111**, 7936 (2014).
  - [11] P. Gallo, K. Amann-Winkel, C. A. Angell, M. A. Anisimov, F. Caupin, C. Chakravarty, E. Lascaris, T. Loerting, A. Z. Panagiotopoulos, J. Russo, J. A. Sellberg, H. E. Stanley, H. Tanaka, C. Vega, L. Xu, and L. G. M. Pettersson, Water: A Tale of Two Liquids, *Chemical Reviews*

- 116**, 7463 (2016).
- [12] P. H. Poole, F. Sciortino, U. Essmann, and H. E. Stanley, Phase behaviour of metastable water, *Nature* **360**, 324 (1992).
- [13] K. H. Kim, A. Späh, H. Pathak, F. Perakis, D. Mariedahl, K. Amann-Winkel, J. A. Sellberg, J. H. Lee, S. Kim, J. Park, K. H. Nam, T. Katayama, and A. Nilsson, Maxima in the thermodynamic response and correlation functions of deeply supercooled water, *Science* **358**, 1589 (2017).
- [14] K. H. Kim, K. Amann-Winkel, N. Giovambattista, A. Späh, F. Perakis, H. Pathak, M. L. Parada, C. Yang, D. Mariedahl, T. Eklund, T. J. Lane, S. You, S. Jeong, M. Weston, J. H. Lee, I. Eom, M. Kim, J. Park, S. H. Chun, P. H. Poole, and A. Nilsson, Experimental observation of the liquid-liquid transition in bulk supercooled water under pressure, *Science* **370**, 978 (2020).
- [15] F. Caupin, V. Holten, C. Qiu, E. Guillerm, M. Wilke, M. Frenz, J. Teixeira, and A. K. Soper, Comment on “Maxima in the thermodynamic response and correlation functions of deeply supercooled water”, *Science* **360**, eaat1634 (2018).
- [16] K. H. Kim, A. Späh, H. Pathak, F. Perakis, D. Mariedahl, K. Amann-Winkel, J. A. Sellberg, J. H. Lee, S. Kim, J. Park, K. H. Nam, T. Katayama, A. Nilsson, F. Caupin, V. Holten, C. Qiu, E. Guillerm, M. Wilke, M. Frenz, J. Teixeira, and A. K. Soper, Response to Comment on “Maxima in the thermodynamic response and correlation functions of deeply supercooled water”, *Science* **360**, eaat1729 (2018).
- [17] P. G. Debenedetti, F. Sciortino, and G. H. Zerze, Second critical point in two realistic models of water, *Science* **369**, 289 (2020).
- [18] J. C. Palmer, P. H. Poole, F. Sciortino, and P. G. Debenedetti, Advances in Computational Studies of the Liquid-Liquid Transition in Water and Water-Like Models, *Chemical Reviews* **118**, 9129 (2018).
- [19] L. Xu, P. Kumar, S. V. Buldyrev, S.-H. Chen, P. H. Poole, F. Sciortino, and H. E. Stanley, Relation between the Widom line and the dynamic crossover in systems with a liquid – liquid phase transition, *Proceedings of the National Academy of Sciences* **102**, 16558 (2005).
- [20] V. V. Vasisht, S. Saw, and S. Sastry, Liquid–liquid critical point in supercooled silicon, *Nature Physics* **7**, 549 (2011).
- [21] M. Beye, F. Sorgenfrei, W. F. Schlotter, W. Wurth, and A. Föhlisch, The liquid-liquid phase transition in silicon revealed by snapshots of valence electrons, *Proceedings of the National Academy of Sciences* **107**, 16772 (2010).
- [22] H. Kanno, H. Yokoyama, and Y. Yoshimura, A New Interpretation of Anomalous Properties of Water Based on Stillinger’s Postulate, *Journal of Physical Chemistry B* **105**, 2019 (2001).
- [23] A. Angell, Thermodynamics: highs and lows in the density of water, *Nature nanotechnology* **2**, 396 (2007).
- [24] H.-S. P. Wong, S. Raoux, S. Kim, J. Liang, J. P. Reifenberg, B. Rajendran, M. Ashghi, and K. E. Goodson, Phase Change Memory, *Proceedings of the IEEE* **98**, 2201 (2010).
- [25] P. Lucas, S. Wei, and C. A. Angell, Liquid-liquid phase transitions in glass-forming systems and their implications for memory technology, *International Journal of Applied Glass Science* **11**, 236 (2020).
- [26] C. Benmore, L. C. Gallington, and E. Soignard, Intermediate range order in supercooled water, *Molecular Physics* **117**, 2470 (2019).
- [27] J. Akola, R. O. Jones, S. Kohara, T. Usuki, and E. Bychkov, Density variations in liquid tellurium: Roles of rings, chains, and cavities, *Physical Review B* **81**, 094202 (2010).
- [28] C. Bergman, C. Bichara, J. P. Gaspard, and Y. Tsuchiya, Experimental investigation of the waterlike density anomaly in the liquid Ge<sub>15</sub>Te<sub>85</sub> eutectic alloy, *Physical Review B* **67**, 104202 (2003).
- [29] J. Kalikka, J. Akola, R. O. Jones, S. Kohara, and T. Usuki, Amorphous Ge<sub>15</sub>Te<sub>85</sub>: density functional, high-energy x-ray and neutron diffraction study, *Journal of Physics: Condensed Matter* **24**, 015802 (2012).
- [30] S. Wei, M. Stolpe, O. Gross, W. Hembree, S. Hechler, J. Bednarcik, R. Busch, and P. Lucas, Structural evolution on medium-range-order during the fragile-strong transition in Ge<sub>15</sub>Te<sub>85</sub>, *Acta Materialia* **129**, 259 (2017).
- [31] J.-P. Gaspard, Structure of covalently bonded materials: From the Peierls distortion to Phase-Change Materials, *Comptes Rendus Physique* **17**, 389 (2016).
- [32] P. Zalden, F. Quirin, M. Schumacher, J. Siegel, S. Wei, A. Koc, M. Nicoul, M. Trigo, P. Andreasson, H. Enquist, M. J. Shu, T. Pardini, M. Chollet, D. Zhu, H. Lemke, I. Ronneberger, J. Larsson, A. M. Lindenberg, H. E. Fischer, S. Hau-Riege, D. A. Reis, R. Mazzarello, M. Wuttig, and K. Sokolowski-Tinten, Femtosecond x-ray diffraction reveals a liquid–liquid phase transition in phase-change materials, *Science* **364**, 1062 (2019).
- [33] B. Cabane and J. Friedel, Local order in liquid tellurium, *Journal de Physique* **32**, 73 (1971).
- [34] Y. Kajihara, M. Inui, K. Matsuda, T. Nagao, and K. Ohara, Density fluctuations at the continuous liquid-liquid phase transition in chalcogen systems, *Physical Review B* **86**, 214202 (2012).
- [35] Y. Tsuchiya, Thermodynamic evidence for a structural transition of liquid Te in the supercooled region, *Journal of Physics: Condensed Matter* **3**, 3163 (1991).
- [36] R. J. Speedy, Thermodynamic properties of supercooled water at 1 atm, *The Journal of Physical Chemistry* **91**, 3354 (1987).
- [37] W. Wagner and A. Pruß, The IAPWS Formulation 1995 for the Thermodynamic Properties of Ordinary Water Substance for General and Scientific Use, *Journal of Physical and Chemical Reference Data* **31**, 387 (2002).
- [38] D. I. Svergun and L. A. Feigin, *Structure Analysis by Small-Angle X-Ray and Neutron Scattering*, edited by G. W. Taylor (Plenum Press, New York, 1987).
- [39] R. J. Speedy, Stability-limit conjecture. An interpretation of the properties of water, *The Journal of Physical Chemistry* **86**, 982 (1982).
- [40] P. H. Poole, F. Sciortino, T. Grande, H. E. Stanley, and C. A. Angell, Effect of Hydrogen Bonds on the Thermodynamic Behavior of Liquid Water, *Physical Review Letters* **73**, 1632 (1994).
- [41] S. Sastry, P. G. Debenedetti, F. Sciortino, and H. E. Stanley, Singularity-free interpretation of the thermodynamics of supercooled water, *Physical Review E* **53**, 6144 (1996).
- [42] K. Stokely, M. G. Mazza, H. E. Stanley, and G. Franzese, Effect of hydrogen bond cooperativity on the behavior of

- water, *Proceedings of the National Academy of Sciences* **107**, 1301 (2010).
- [43] F. Caupin and M. A. Anisimov, Minimal Microscopic Model for Liquid Polyamorphism and Waterlike Anomalies, *Physical Review Letters* **127**, 185701 (2021).
- [44] H. Endo, K. Maruyama, H. Hoshino, and H. Ikemoto, Local Structure of Liquid Te Studied by Neutron Diffraction and EXAFS, *Zeitschrift für Physikalische Chemie* **217**, 863 (2003).
- [45] A. Menelle, R. Bellissent, and A. M. Flank, A Neutron Scattering Study of Supercooled Liquid Tellurium, *Europhysics Letters* **4**, 705 (1987).
- [46] T. Ichikawa, Electron Diffraction Study of the Local Atomic Arrangement in Amorphous Tellurium Films, *physica status solidi (b)* **56**, 707 (1973).
- [47] T. Tsuzuki, M. Yao, and H. Endo, Static and Dynamic Structures of Liquid Tellurium, *Journal of the Physical Society of Japan* **64**, 485 (1995).
- [48] A. Menelle, R. Bellissent, and A. M. Flank, Short range order in liquid Se-Te system by neutron scattering, *Physica B: Physics of Condensed Matter* **156-157**, 174 (1989).
- [49] W. Hoyer, H. Neumann, and M. Wobst, Structure Investigation on Liquid Tellurium by X-Ray and Neutron Scattering, *Zeitschrift für Naturforschung A* **47**, 833 (1992).
- [50] C. Adenis, V. Langer, and O. Lindqvist, Reinvestigation of the structure of tellurium, *Acta Crystallographica C* **45**, 941 (1989).
- [51] H. Tanaka, Bond orientational order in liquids: Towards a unified description of water-like anomalies, liquid-liquid transition, glass transition, and crystallization, *European Physical Journal E* **35**, 113 (2012).

# Supplementary Materials

(Dated: January 19, 2022)

## I. MATERIALS AND METHODS

The samples used in this study are Te powder (99.999% metals basis, purchased from Alfa Aesar) vacuum-sealed in borosilicate glass ampoules. The inner diameter of the glass container is around 0.7 mm, and its wall thickness is around 0.085 mm.

Figure S2 shows a schematics of the experimental setup used at beamline 1-ID at the Advanced Photon Source. The sample is placed in a hollow cylindrical oven wrapped in resistive heater wires. At the center of the tube, a through path is created for both the entrance and the exit of X-rays. A control thermocouple (TC) is inserted into a fixed location in the oven. Downstream from the sample is placed, in sequence, a WAXS detector (GE 41RT [1]), a helium flight tube, a beamstop (with a diode at the center to measure the transmitted beam intensity,  $I_1$ ), and a SAXS detector (Pixirad2). Another diode (not shown),  $I_0$ , is placed before the sample and measures the incoming beam intensity.

The planes of the WAXS and SAXS detectors are 2.003 m and 6.420 m from the sample, respectively. The  $Q$ -positions of the WAXS detector pixels are calibrated using a  $\text{CeO}_2$  powder sample.

## II. TEMPERATURE CALIBRATION

Due to the opening in the center of the oven for the passage of the X-rays, some temperature gradient is expected within the oven. In order to calibrate the sample temperature, we measure the melting of three materials, Bi, Te, and Sb, with the WAXS pattern. The temperature of the control TC is increased in small steps, and WAXS patterns are collected after equilibration at each step. Melting can be observed unambiguously as the disappearance of sharp Bragg peaks and the appearance of a halo pattern. The corresponding control TC temperature can be determined within 5 K. In Fig. S3 we plot the temperature of the control TC thus determined against the melting temperature of each sample. The data are well described by the linear fit shown in the plot, and we use the fit result for the analysis. We note that the calibrated temperature range well covers the range used in our Te measurements, from above 580 K to below 750 K.

Another way to cross-check the temperature calibration and ensure consistency between different scans is through the position of the first peak of the liquid,  $Q_{m1}$ . This quantity depends sensitively on the sample temperature and can be determined with a high accuracy because of the relatively strong WAXS signal. In addition, it is independent of normalization and insensitive to possible smooth changes in the background.

In Fig. S4, we plot  $Q_{m1}$  against the calibrated sample

temperature. We can see that data from different scans align well with each other. From these data, the temperature derivative of  $Q_{m1}$  is calculated and plotted in Fig. 3c in the main text.

## III. DENSITY MEASUREMENTS

The density of the sample is determined *via* X-ray transmission measurements. Experimentally, we measure the incoming X-ray intensity  $I_0$  and transmitted beam intensity  $I_1$  at each sample temperature. The same measurements are also done with an empty capillary, giving the background values  $I_0^{\text{bg}}$  and  $I_1^{\text{bg}}$ . We then have:

$$\frac{I_1}{I_1^{\text{bg}}} = \frac{I_0}{I_0^{\text{bg}}} \exp[-(\mu/\rho)\rho t], \quad (\text{S1})$$

where  $\mu/\rho$  is the mass attenuation coefficient of the sample,  $\rho$  its density, and  $t$  its thickness. For tellurium and an X-ray energy of 76.112 keV,  $\mu/\rho = 3.68 \text{ cm}^2/\text{g}$  [2].

With measured values of  $I_0$ ,  $I_1$ ,  $I_0^{\text{bg}}$ , and  $I_1^{\text{bg}}$ , Eq. (S1) describes a relation between  $\rho$  and  $t$ . Since  $t$  depends on both the sample and the beam position, it may change between scans. Thus, for each cycle,  $t$  is determined using the literature value of  $\rho$  at the highest temperature [3]. The density  $\rho$  at the other temperatures in the cycle can then be determined given this value of  $t$ . As can be seen in Fig. S5c below and Fig. 2 in the main text, the results from different cycles and different scans are consistent with each other, and all agree well with the values reported by Tsuchiya [3]. This also indicates that sample movement is minimal during each cycle.

## IV. CONSISTENCY BETWEEN CYCLES

As mentioned in the main text, each one of the three scans in our dataset consists of several cycles. In each cycle, the sample is first heated above its melting point and then cooled down in steps (usually 10 K) to the lowest temperature. We take scan 1 as an example to demonstrate the consistency between data from different cycles, and the results are shown in Fig. S5. Because of a high signal-to-noise ratio, the WAXS data from different cycles overlap well with each other, as shown in Fig. S5a-b. The density measurements based on X-ray transmission are also well reproduced between cycles, as shown in Fig. S5c.

In comparison, the SAXS signal is weaker and somewhat larger variations are observed between cycles, but the data remain consistent. As mentioned in the main text, in the analysis, the SAXS data at the highest temperature of each cycle (733 K in this scan) is subtracted

from the data at other temperatures, and we analyze the difference

$$\Delta S(Q) = S(Q) - S(Q; T = 733 \text{ K}). \quad (\text{S2})$$

Figure S5d shows  $\Delta S(Q)$  integrated from  $Q = 0.06 \text{ \AA}^{-1}$  to  $0.15 \text{ \AA}^{-1}$ ; the black crosses show the average values, with error bars representing the standard error of the mean. We then fit  $\Delta S(Q)$  with a linear function:

$$\Delta S(Q) = \Delta S(0) - kQ. \quad (\text{S3})$$

The  $Q = 0$  intercept,  $\Delta S(0)$ , and the slope  $k$  extracted from the fit are shown in Fig. S5e and f, respectively. The same trend can be observed in panels (d), (e), and (f), where a maximum around 615 K can be observed. The intercept  $\Delta S(0)$  is reported in the main text and used for further analysis.

## V. WAXS ANALYSIS DETAILS

This section shows details of the WAXS data analysis. To obtain  $S(Q)$ , we first calculate the azimuthally integrated intensity profile  $I(Q)$  from the WAXS images. Next, we subtract the background measured with an empty glass ampoule without sample; the background consists of two parts, one coming from air scattering before the sample which is not affected by the sample, and one from the glass capillary and air scattering after the sample which is scaled by the X-ray transmission through the sample. We then normalize the curve, subtract the Compton scattering as well as a flat fluorescence background, and divide the data by the form factor  $|f(Q)|^2$  to obtain the  $S(Q)$  data. The resulting  $S(Q)$  data for  $T = 724 \text{ K}$  are shown in Fig. S6a as blue dots. Because a small amount of tellurium oxide is present, the data contain some weak powder rings which appear as sharp peaks in  $S(Q)$ . These outliers can be identified and excluded, resulting in the smoothed data shown as the red line, which agrees well with the X-ray data at 723 K reported by Akola et al. [4]. The latter is also shown [4] to agree well with earlier neutron data by Menelle et al. [5].

For our WAXS dataset, the measured  $Q$ -range is from around  $0.8 \text{ \AA}^{-1}$  to  $7 \text{ \AA}^{-1}$ . However, it can be seen that [4], across the wide temperature range from 623 K to 1123 K, very little change occurs in  $S(Q)$  above  $6 \text{ \AA}^{-1}$ . A similar observation can be made based on the data reported by Endo et al. [6] which included a smaller  $Q$ - and temperature-range. Therefore, in order to more accurately calculate the radial distribution function,  $g(r)$ , we append the previously reported data [4] of  $S(Q)$  from  $7 \text{ \AA}^{-1}$  to  $15 \text{ \AA}^{-1}$  to our results before integration. On the low- $Q$  side, a linear interpolation is used for the reduced structure function,  $Q[S(Q) - 1]$ , between  $0 \text{ \AA}^{-1}$  and  $0.8 \text{ \AA}^{-1}$  before integration (see Fig. S6b). The result at  $T = 724 \text{ K}$  can be compared with that at 723 K

reported by Akola et al. [4], as shown in Fig. S6. A good agreement can be observed between the present data and previous results.

In Fig. S7, we show the same results at 626 K, compared with the neutron diffraction data at 623 K reported by Menelle et al. [4, 5].

## VI. PRE-PEAK ANALYSIS

In this section, we present quantitative results on the pre-peak observed in the WAXS data as shown in Fig. 1a in the main text. After subtracting the baseline, the data can be fit well with a Gaussian function, whereby the center,  $Q_{pp}$ , and the integrated intensity under the Gaussian,  $I_{pp}$ , can be extracted. The results are shown in Fig. S8a-b, and their temperature derivatives in Fig. S8c-d. Note that the amplitude of the pre-peak is small, as can be seen in Fig. 1a, so small changes in the background could lead to errors. Nonetheless, the presence of a maximum is apparent in the temperature derivative of both  $Q_{pp}$  and  $I_{pp}$ , suggesting effects of the Widom line. The peak temperature of  $dI_{pp}/dT$ ,  $\sim 640 \text{ K}$ , is somewhat higher than the Widom line position based on the isothermal compressibility maximum, around 615 K (see Fig. 3 in the main text). However, the  $\sim 25 \text{ K}$  difference is small compared to the full-width at half-maximum of the peak, which is more than 100 K.

Remarkably, although the pre-peak is present even above the melting point, its growth in intensity upon cooling is rather significant: as shown in Fig. S8b,  $I_{pp}$  increases from  $0.012 \text{ \AA}^{-1}$  at 738 K to  $0.020 \text{ \AA}^{-1}$  at 585 K, i.e., by more than 60%.

## VII. BOUNDARIES OF THE INTERMEDIATE REGION

In the main text, we have used  $R_1 = 3.14 \text{ \AA}$  and  $R_2 = 3.69 \text{ \AA}$  as the lower and upper boundaries of the intermediate region. Here, we show that the conclusions, in particular the rapid change in  $N_{\text{int}}$  around the Widom line, do not depend sensitively on the definition of the boundaries. To test this, we change the value of  $R_1$  or  $R_2$  by  $\pm 0.2 \text{ \AA}$ , and calculate the number of atoms for each pair of  $R_1$  and  $R_2$ . The results are shown in Fig. S9. Although different choices lead to different  $N_{\text{int}}$  values (see Fig. S9b), the derivatives all show a peak around the Widom line position (see Fig. S9c).

## VIII. SAXS AND WAXS DATA FOR ALL SCANS

In Figs. S10 and S11, we show details of the WAXS and SAXS data for scans 2 and 3, respectively. The SAXS data in these scans show larger error bars because of lower signal levels, but the results are consistent with those from scan 1 shown in the main text.

The WAXS results for all three scans, including the calculated  $g(r)$ , are presented in Figs. S12 to S14. The results are consistent between different scans.

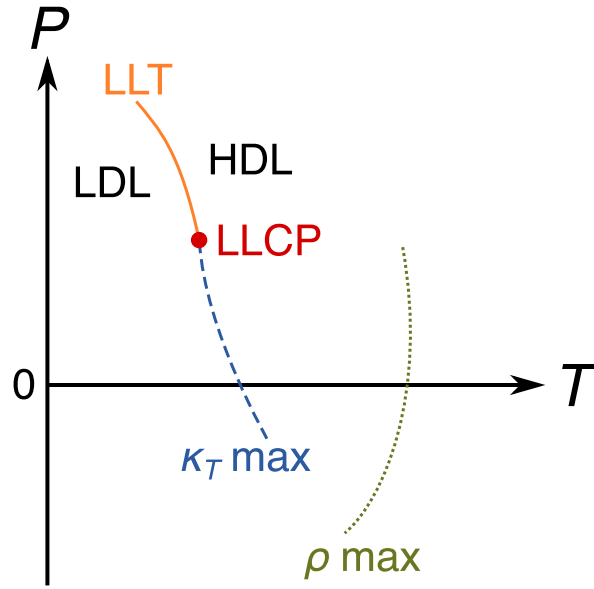


FIG. S1. Schematics of a likely phase diagram of liquid water [7–9]. The line of liquid-liquid transition (LLT) separates the low-density (LDL) and high-density liquid (HDL) phases. The LLT ends at a liquid-liquid critical point (LLCP), with a critical pressure expected to be on the order of one to a few kilobars [9, 10]. From the LLCP emanates the line of isothermal compressibility maxima along isobars ( $\kappa_T$  max), which intersects the  $P \approx 0$  isobar around 229 K [9]. Also shown is the line of density maxima along isobars ( $\rho$  max), which is known to intersect  $P = 1$  bar at  $T = 277$  K. Our study suggests that a similar phase diagram is expected for liquid Te.

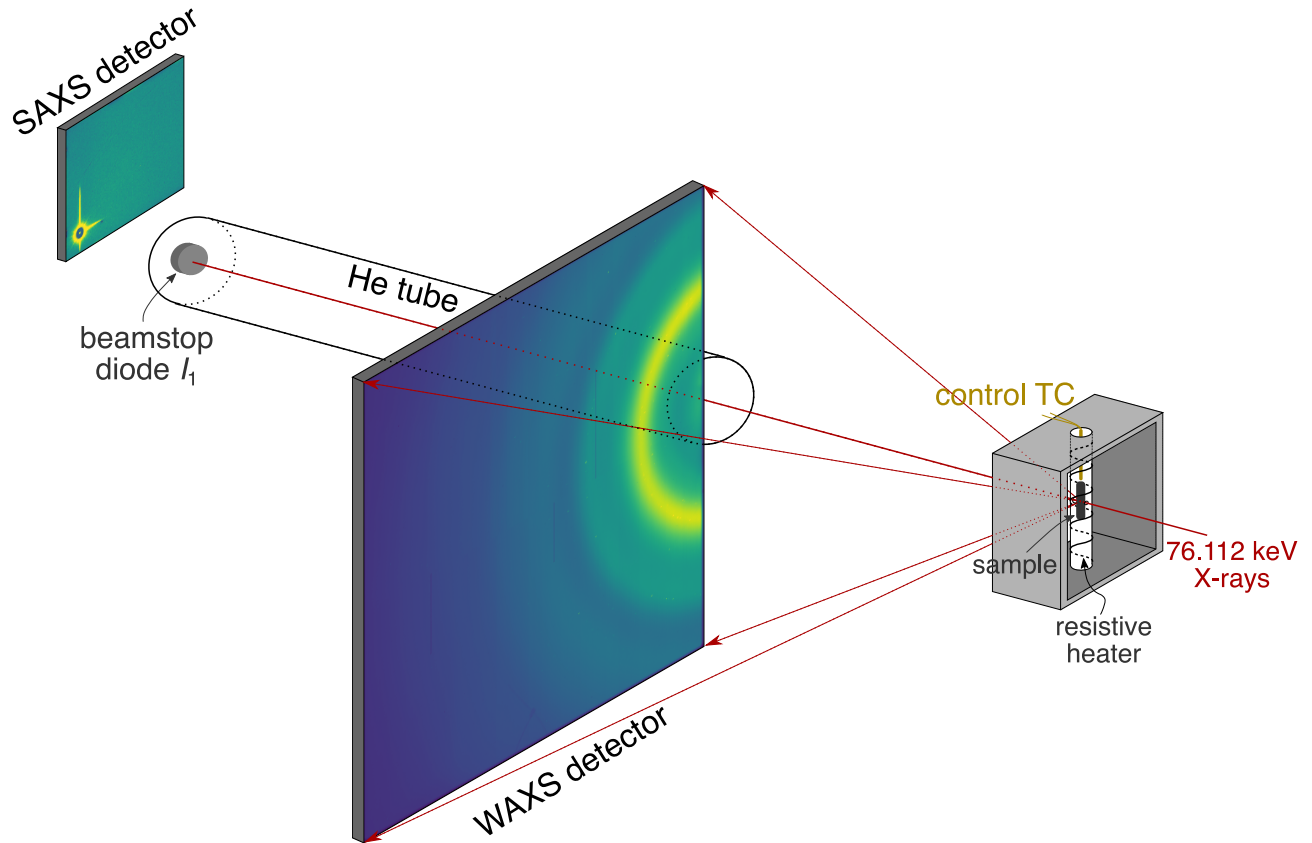


FIG. S2. Experimental setup (not to scale).

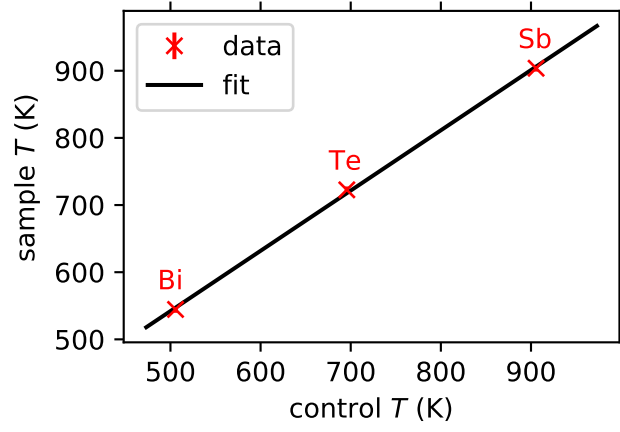


FIG. S3. Temperature calibration. The red crosses show the temperature reading of the control TC at melting plotted against the actual melting temperature for each sample. The solid black line shows a linear fit.

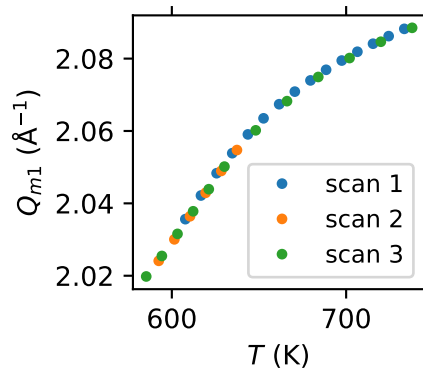


FIG. S4. Position of the first peak,  $Q_{m1}$ , plotted against the calibrated sample temperature,  $T$ , for all three scans.

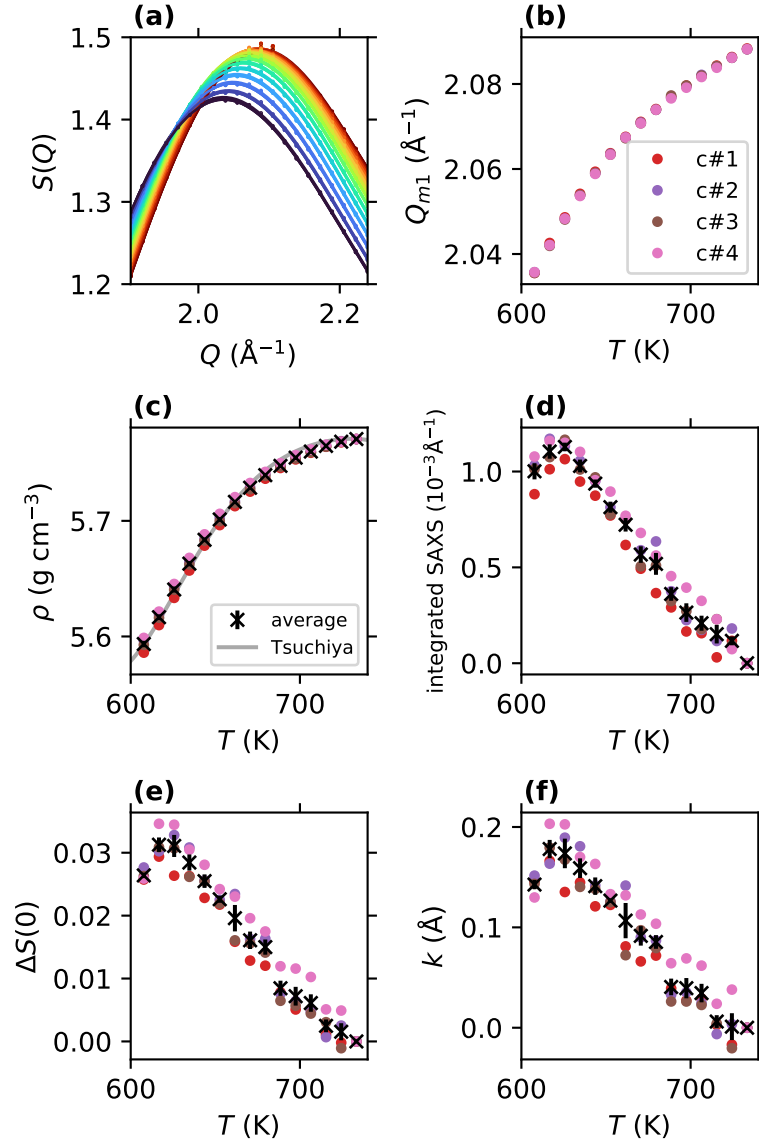


FIG. S5. Consistency of data from different cycles in scan 1. (a) Dots: WAXS data around the first peak; lines: fit to the data with a Gaussian function and a linear background. From dark red to dark blue the temperature decreases from 733 K to 608 K, same as Fig. 1 in the main text. Data and fits for all four cycles are shown, and the results well overlap. (b) The position of the first peak,  $Q_{m1}$ , extracted from the fits. The symbols representing different cycles overlap. (c) Density  $\rho$  based on X-ray transmission measurements; also shown are the average (black crosses with error bars) as well as the results reported by Tsuchiya [3] (gray line). (d) SAXS data  $\Delta S(Q)$  integrated from  $0.06 \text{\AA}^{-1}$  to  $0.15 \text{\AA}^{-1}$ . (e) The intercept  $\Delta S(0)$  and (f) the slope  $k$  extracted from the linear fit to  $\Delta S(Q)$ .

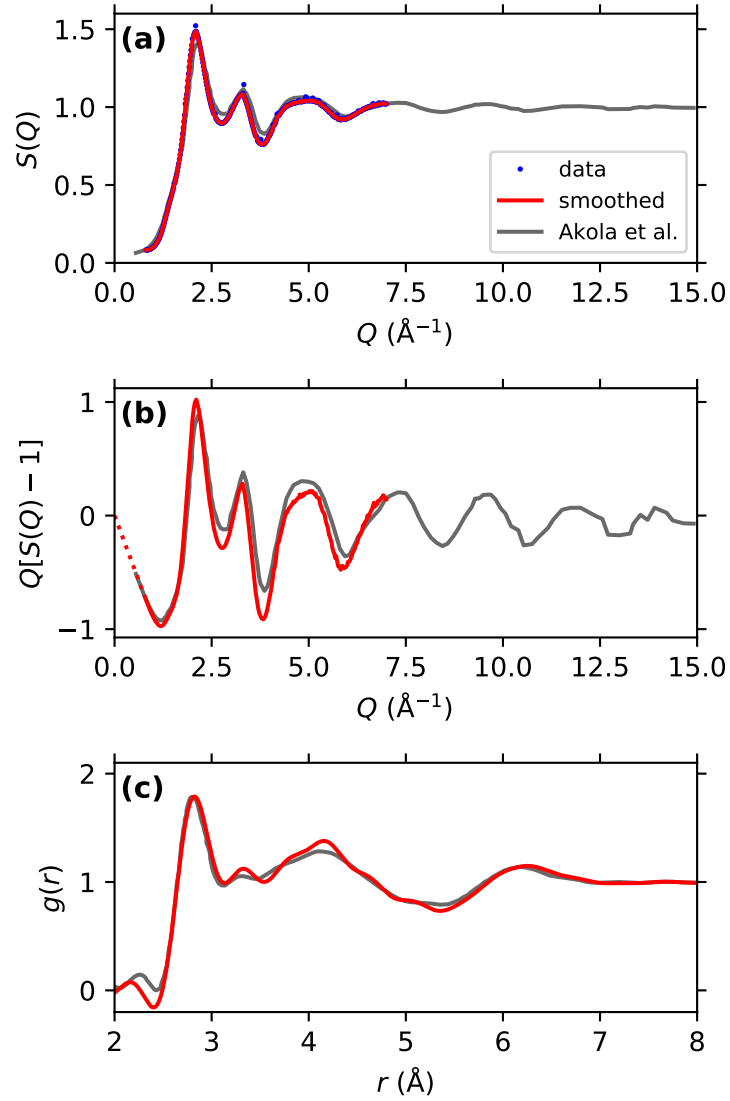


FIG. S6. WAXS analysis. (a) Structure factor  $S(Q)$ . Blue dots: data at  $T = 724$  K. Red line: smoothed data after exclusion of sharp peaks. Gray line: X-ray diffraction data at 723 K reported by Akola et al. [4]. (b) Reduced structure function,  $Q[S(Q) - 1]$ . The dotted part shows the low- $Q$  extension used in the calculation of the radial distribution function,  $g(r)$ , shown in (c).

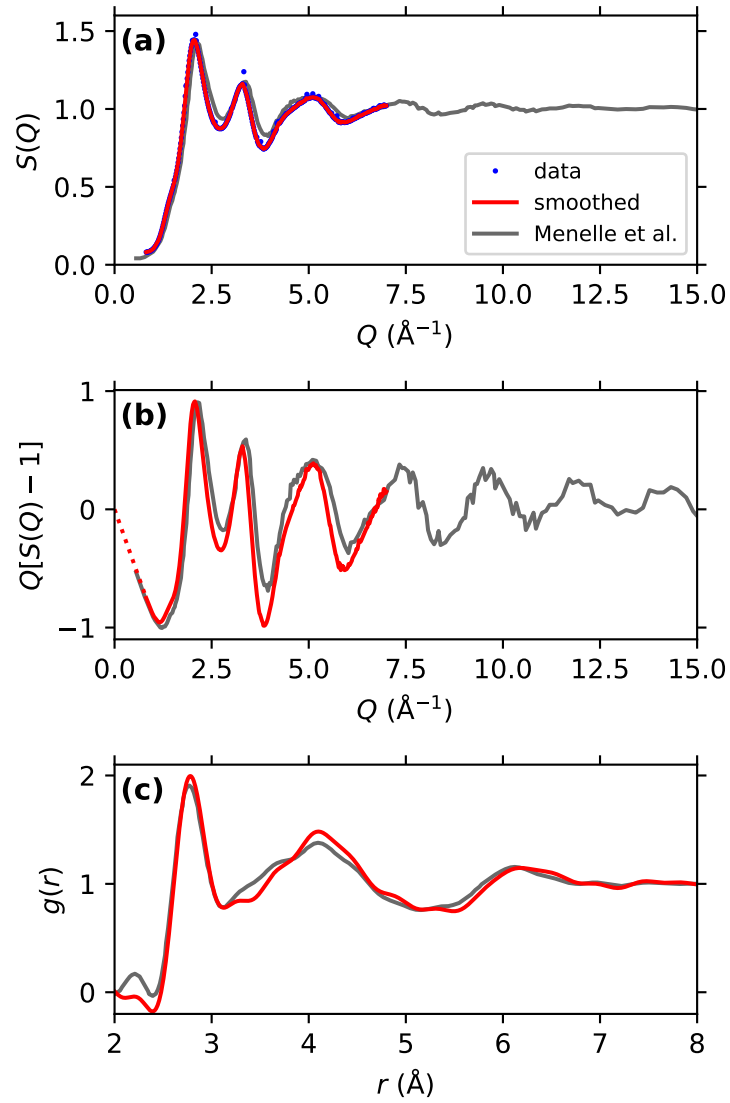


FIG. S7. Same as Fig. S6 but for  $T = 626$  K, compared with neutron diffraction data at 623 K reported by Menelle et al. [4, 5].

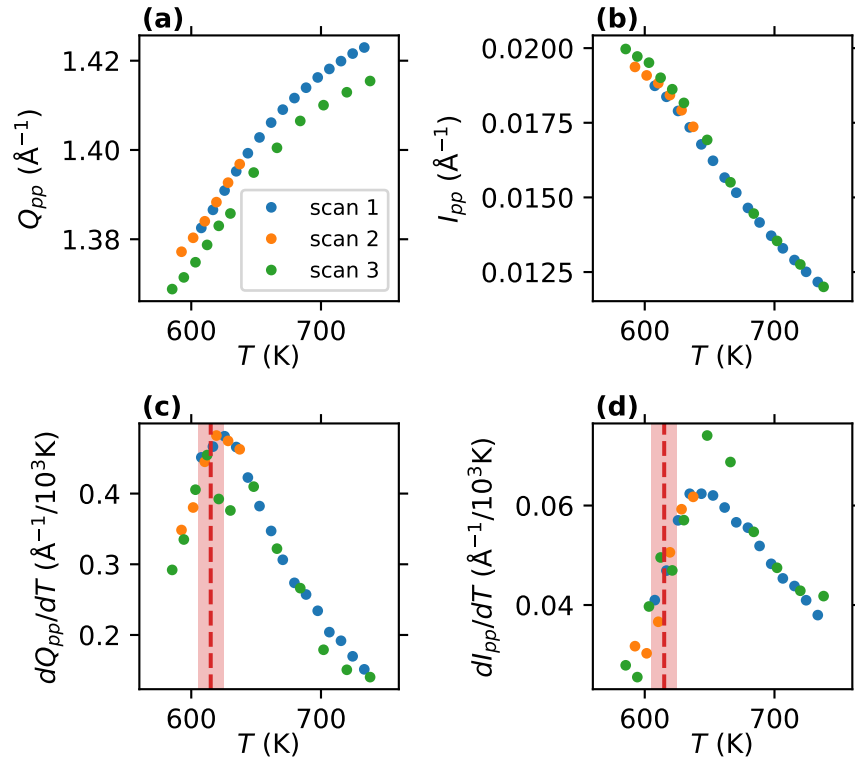


FIG. S8. (a) The center position,  $Q_{pp}$ , and (b) the integrated intensity,  $I_{pp}$ , of the pre-peak, plotted against sample temperature. (c) and (d) show their temperature derivatives. The dashed vertical line shows the position of the Widom line, 615 K, based on the isothermal compressibility.

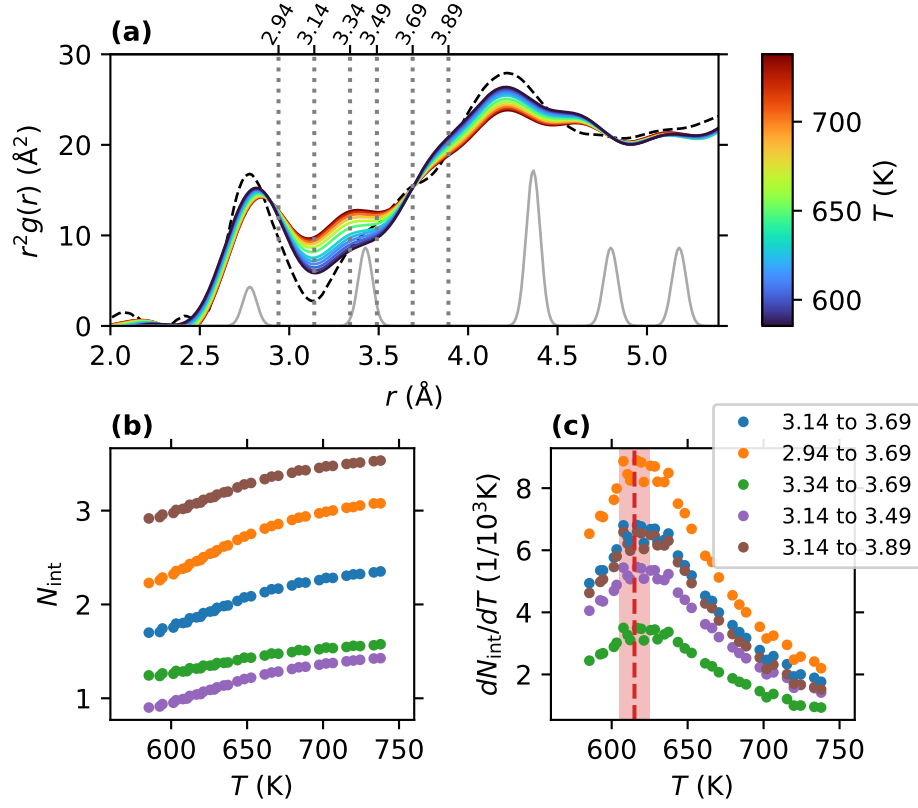


FIG. S9. Test of the boundaries of the intermediate region. (a) The function  $r^2g(r)$ . Colored solid lines: liquid Te from scan 3, from dark red to dark blue are decreasing temperatures from 738 K to 585 K, as shown in the color bar. Also shown are trigonal Te [11] (gray solid line) and electron diffraction results on amorphous Te [12] (black dashed line). Vertical dashed lines indicate different values of  $R_1$  and  $R_2$ ; the values are shown on the upper  $x$ -axis. (b) The number of atoms between  $R_1$  and  $R_2$ , and (c) its temperature derivative. Different colors represent different choices of  $R_1$  and  $R_2$ , as shown in the legend. Data from all three scans are included. Blue dots ( $R_1 = 3.14$  Å,  $R_2 = 3.69$  Å) correspond to the choice in the main text. The derivatives show a maximum near the Widom line (dashed vertical line), independent of the choice.

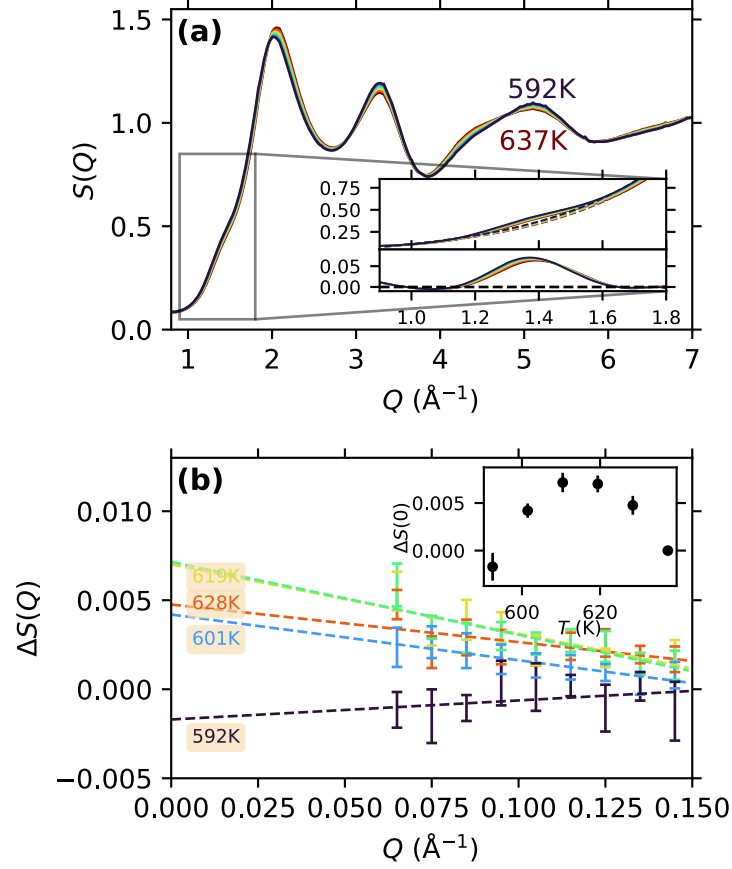


FIG. S10. Same as Fig. 1 in the main text, but for scan 2. (a) Te WAXS profiles (structure factor  $S(Q)$ ) from scan 2. From dark red to dark blue is decreasing temperature; the highest and lowest temperatures are indicated. Inset: upper panel shows the details of the pre-peak around  $1.4 \text{ \AA}^{-1}$  (solid lines) and the background (dashed lines) obtained by fitting data before and after the pre-peak; lower panel shows the pre-peak with the background subtracted. (b) Te SAXS profiles from the same scan, subtracting the highest temperature profile (628 K) in the scan. The color scheme is the same as in (a). Data are shown with error bars, and the dashed lines show a linear fit to the data. Selected temperatures are marked next to the fit lines with the corresponding colors. Inset shows the intercept  $\Delta S(0)$  plotted against sample temperature.

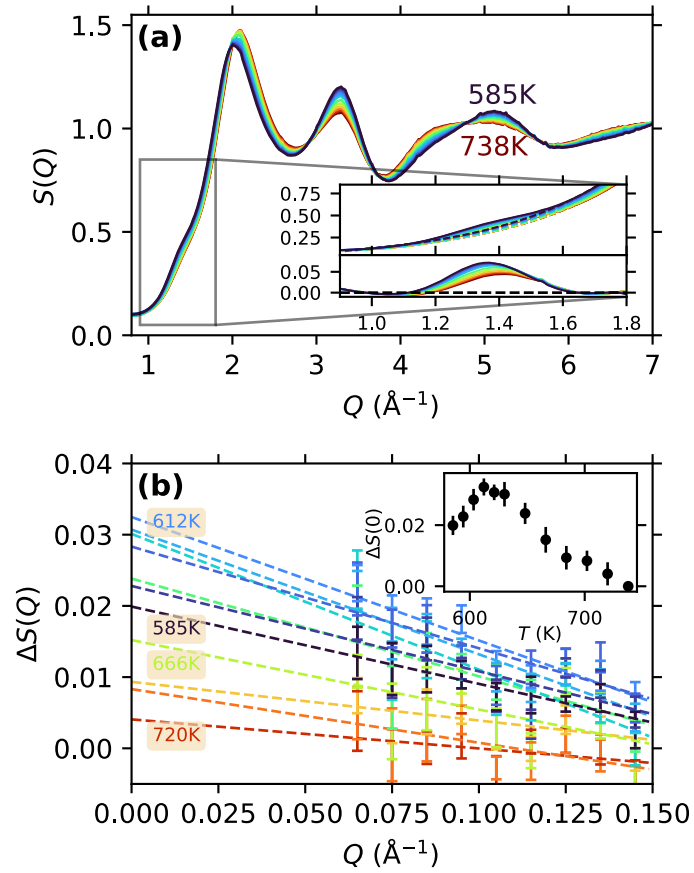


FIG. S11. Same as Fig. S10, but for scan 3.

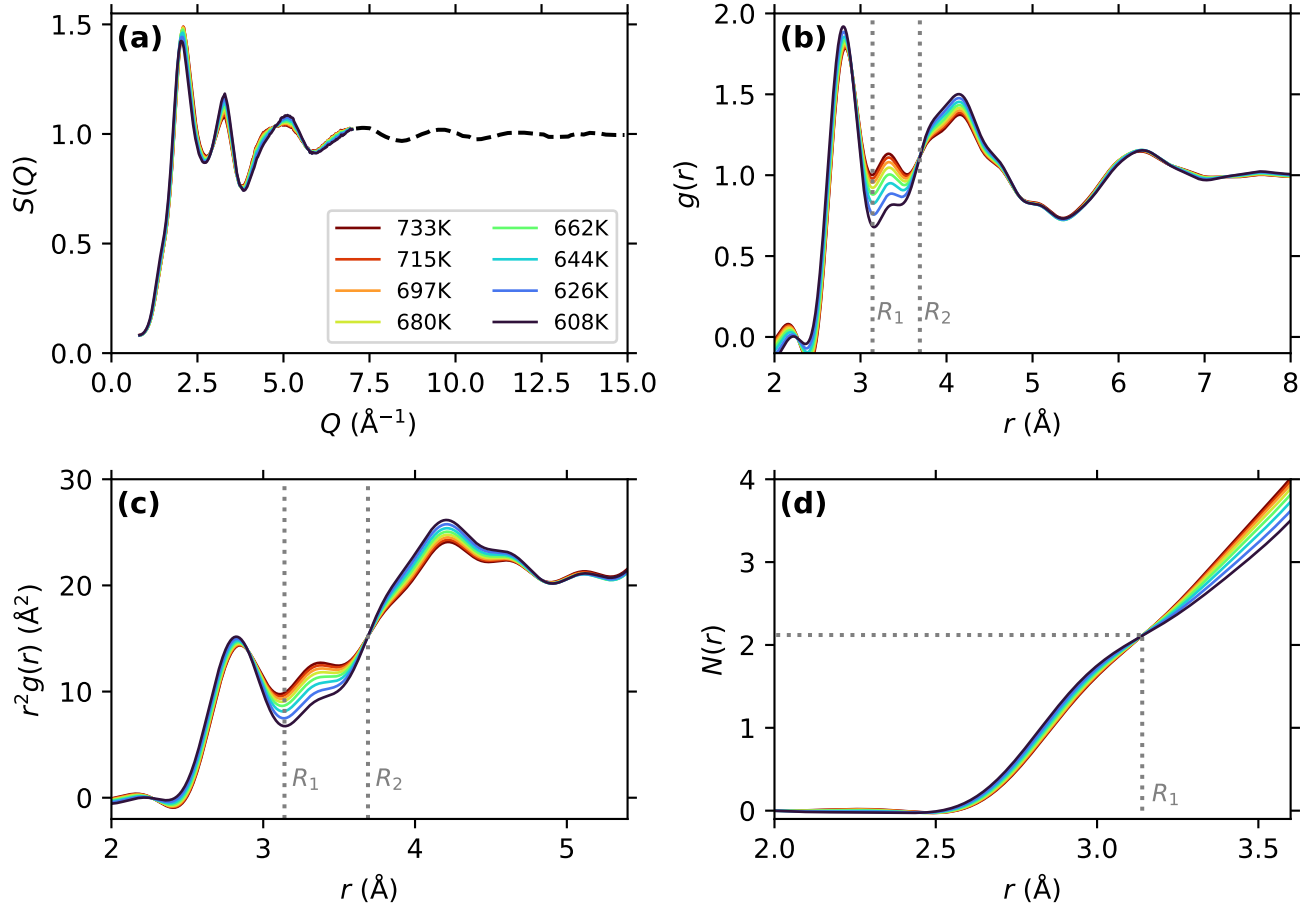


FIG. S12. WAXS results for scan 1. (a) Structure factor  $S(Q)$ . The appended data [4] from  $7 \text{\AA}^{-1}$  to  $15 \text{\AA}^{-1}$  is shown as dashed black line. (b) Radial distribution function  $g(r)$ . Dotted vertical lines shows the boundary of the intermediate region,  $R_1$  and  $R_2$ , as discussed in the main text. (c) The function  $r^2g(r)$ . (d) Running coordination number  $N(r)$ .

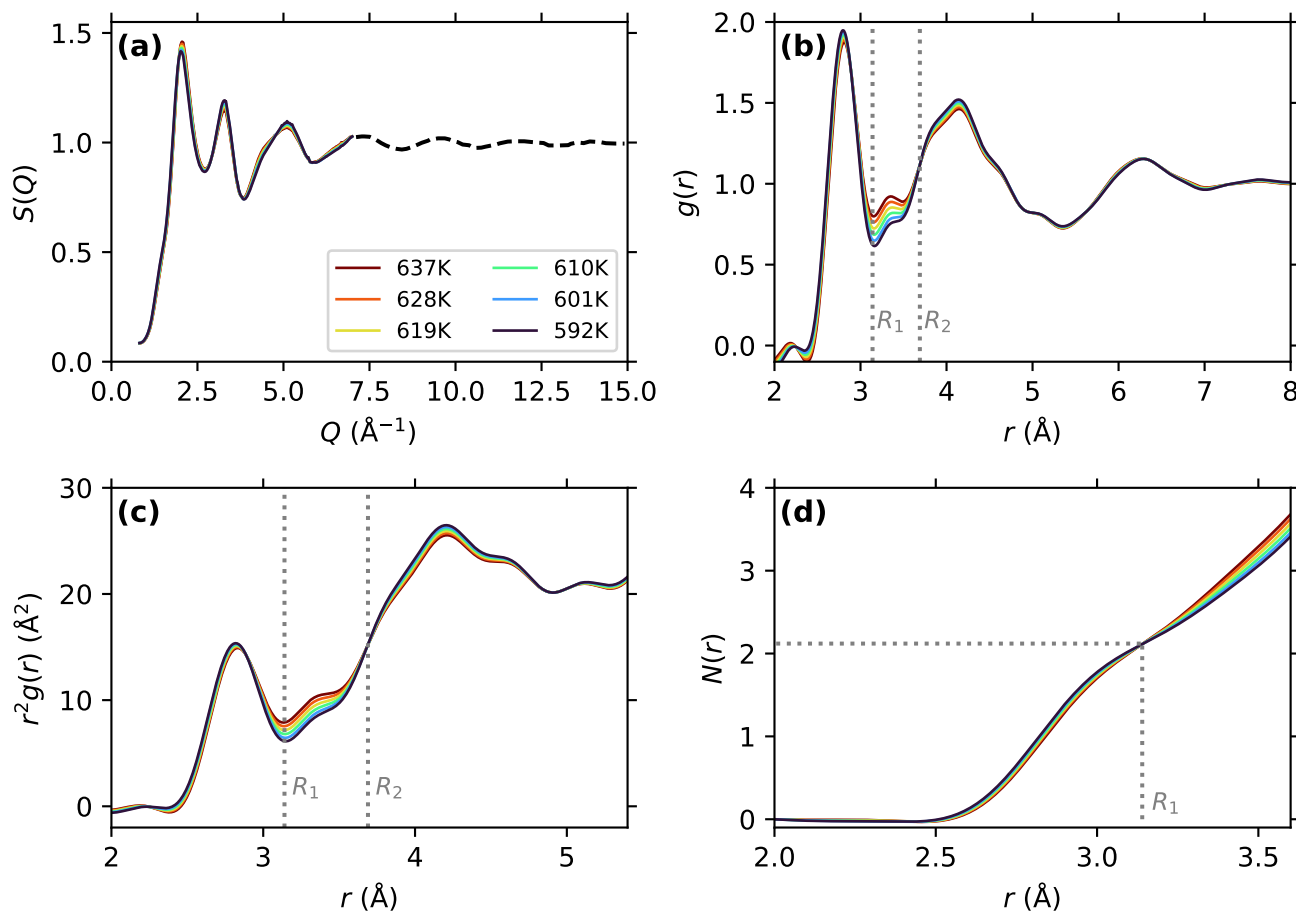


FIG. S13. WAXS results for scan 2. Same as Fig. S12.

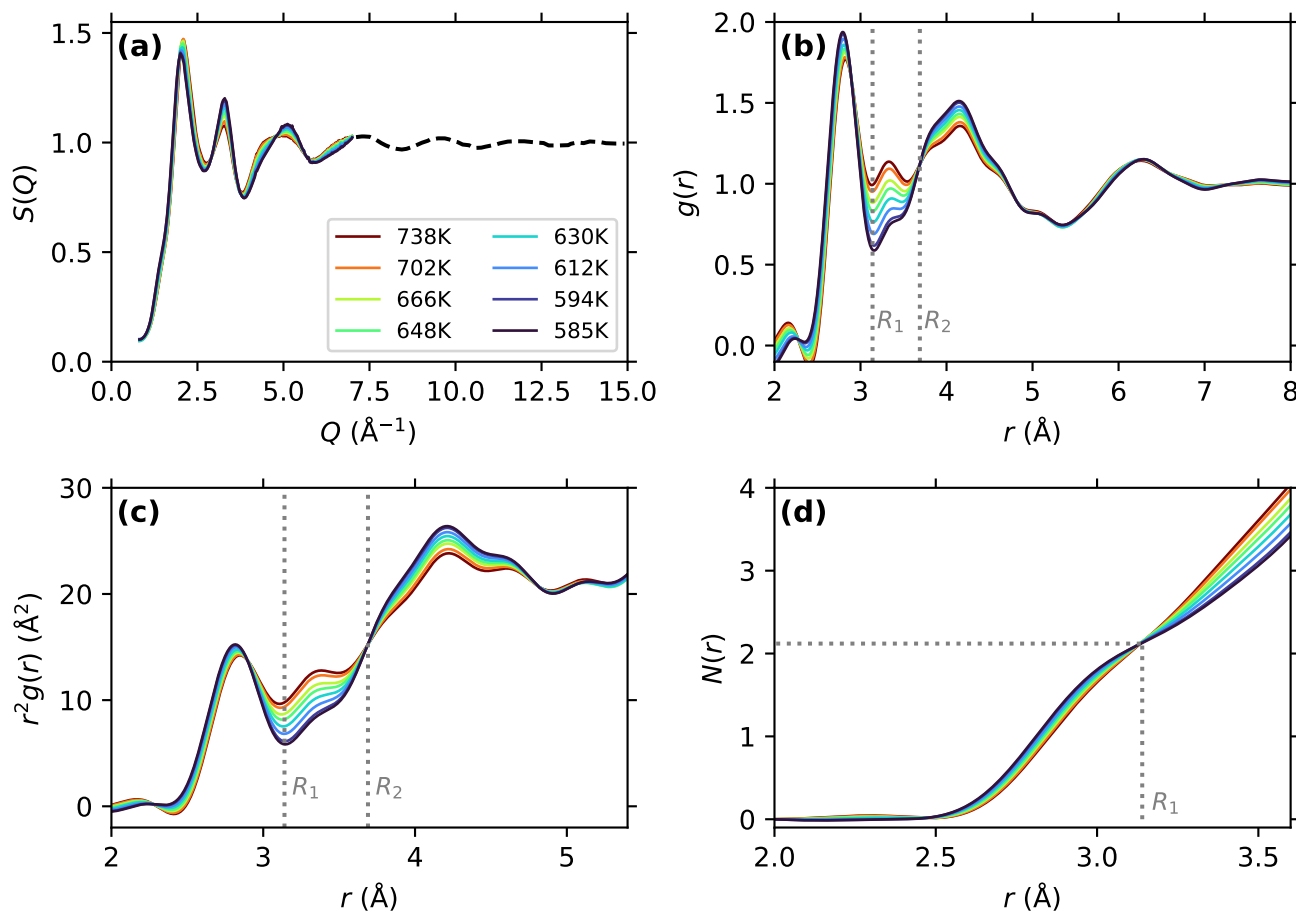


FIG. S14. WAXS results for scan 3. Same as Fig. S12.

- 
- [1] J. H. Lee, C. C. Aydiner, J. Almer, J. Bernier, K. W. Chapman, P. J. Chupas, D. Haefner, K. Kump, P. L. Lee, U. Lienert, A. Miceli, and G. Vera, Synchrotron applications of an amorphous silicon flat-panel detector, *Journal of Synchrotron Radiation* **15**, 477 (2008).
- [2] C. T. Chantler, Theoretical Form Factor, Attenuation, and Scattering Tabulation for  $Z=1-92$  from  $E=1-10$  eV to  $E=0.4-1.0$  MeV, *Journal of Physical and Chemical Reference Data* **24**, 71 (1995).
- [3] Y. Tsuchiya, Thermodynamic evidence for a structural transition of liquid Te in the supercooled region, *Journal of Physics: Condensed Matter* **3**, 3163 (1991).
- [4] J. Akola, R. O. Jones, S. Kohara, T. Usuki, and E. Bychkov, Density variations in liquid tellurium: Roles of rings, chains, and cavities, *Physical Review B* **81**, 094202 (2010).
- [5] A. Menelle, R. Bellissent, and A. M. Flank, Short range order in liquid Se-Te system by neutron scattering, *Physica B: Physics of Condensed Matter* **156-157**, 174 (1989).
- [6] H. Endo, K. Maruyama, H. Hoshino, and H. Ikemoto, Local Structure of Liquid Te Studied by Neutron Diffraction and EXAFS, *Zeitschrift für Physikalische Chemie* **217**, 863 (2003).
- [7] G. Pallares, M. El Mekki Azouzi, M. A. Gonzalez, J. L. Aragonés, J. L. F. Abascal, C. Valeriani, and F. Caupin, Anomalies in bulk supercooled water at negative pressure, *Proceedings of the National Academy of Sciences* **111**, 7936 (2014).
- [8] P. Gallo, K. Amann-Winkel, C. A. Angell, M. A. Anisimov, F. Caupin, C. Chakravarty, E. Lascaris, T. Loerting, A. Z. Panagiotopoulos, J. Russo, J. A. Sellberg, H. E. Stanley, H. Tanaka, C. Vega, L. Xu, and L. G. M. Pettersson, Water: A Tale of Two Liquids, *Chemical Reviews* **116**, 7463 (2016).
- [9] K. H. Kim, A. Späh, H. Pathak, F. Perakis, D. Mariedahl, K. Amann-Winkel, J. A. Sellberg, J. H. Lee, S. Kim, J. Park, K. H. Nam, T. Katayama, and A. Nilsson, Maxima in the thermodynamic response and correlation functions of deeply supercooled water, *Science* **358**, 1589 (2017).
- [10] K. H. Kim, K. Amann-Winkel, N. Giovambattista, A. Späh, F. Perakis, H. Pathak, M. L. Parada, C. Yang, D. Mariedahl, T. Eklund, T. J. Lane, S. You, S. Jeong, M. Weston, J. H. Lee, I. Eom, M. Kim, J. Park, S. H. Chun, P. H. Poole, and A. Nilsson, Experimental observation of the liquid-liquid transition in bulk supercooled water under pressure, *Science* **370**, 978 (2020).
- [11] C. Adenis, V. Langer, and O. Lindqvist, Reinvestigation of the structure of tellurium, *Acta Crystallographica C* **45**, 941 (1989).
- [12] T. Ichikawa, Electron Diffraction Study of the Local Atomic Arrangement in Amorphous Tellurium Films, *physica status solidi (b)* **56**, 707 (1973).